Advances in Applied Mathematics and Mechanics
Adv. Appl. Math. Mech., Vol. **2**, No. 1, pp. 1-31

DOI: 10.4208/aamm.09-m0938
February 2010

Nonlinear Viscoelastic Response of Thermoplastic–Elastomer Melts

Aleksey D. Drozdov[1,*], Erik A. Jensen[2] and Jesper deClaville Christiansen[2]

[1] *Danish Technological Institute, Gregersensvej 1, 2630 Taastrup, Denmark*

[2] *Aalborg University, Fibigerstraede 16, 9220 Aalborg, Denmark*

Received 13 May 2009; Accepted (in revised version) 06 July 2009
Available online 31 December 2009

Abstract. Observations are reported on thermoplastic elastomer (ethylene-octene copolymer) melt in small-amplitude shear oscillatory tests and start-up shear tests with various strain rates in the interval of temperatures between 120 and 210 °C. Based on the concept of heterogeneous non-affine polymer networks, constitutive equations are developed for the thermo-mechanical behavior of a melt at three-dimensional deformations with finite strains. Adjustable parameters in the stress–strain relations are found by fitting the experimental data. The model is applied to the analysis of Poiseuille flow. The effects of temperature and pressure gradient on the steady velocity profile are studied numerically.

AMS subject classifications: 74A20, 76A10, 76D07

Key words: Non-affine polymer network, thermo-viscoelasticity, elastomer melt, constitutive model, Poiseuille flow.

1 Introduction

This paper deals with the experimental investigation and constitutive modeling of the nonlinear thermo-viscoelastic response of thermoplastic-elastomer (TPE) melts at three-dimensional deformations with finite strains. Modeling the time–dependent behavior of polymer melts has been a focus of attention in the past three decades. Among constitutive equations for the viscoelastic and viscoplastic responses of polymer melts, it is worth mentioning (i) the Leonov model [1], (ii) the Johnson–Segalman model [2], (iii) the Phan Thien–Tanner model [3], (iv) the Wagner model (a modification of the

*Corresponding author.
URL: `www.tejknologisk.dk`
Email: Aleksey.Drozdov@teknologisk.dk (A. D. Drozdov), erikappel@gmail.com (E. A. Jensen), jc@production.aau.dk (J. deC. Christiansen)

K–BKZ constitutive equations) [4], (v) the Giesekus model [5], (vi) the finitely extensible nonlinear elastic (FENE) network model [6], (vii) the pom–pom model [7], (viii) the reptation model with incorporation of segmental stretching [8], and (ix) molecular stress function model [9], to mention a few.

The present study focuses on the nonlinear thermo-viscoelastic behavior of a thermoplastic elastomer (ethylene-octene random copolymer) melt in conventional (i) oscillatory shear tests with small amplitudes and (ii) start-up shear tests with constant strain rates at various temperatures. Rheology of ethylene-octene copolymer melts has attracted substantial attention in the past decade (see [10]– [19]) for two reasons. First, these polymers with large concentrations of higher olefin comonomers (above 20 wt.-%) are widely used as rubber modifiers for thermoplastics [15]. Secondly, ethylene copolymers produced by metallocene catalysis have relatively low polydispersity and contain long chain branches that strongly affect their properties. In particular, (i) the zero-shear viscosity and (ii) the apparent flow activation energy of polyethylenes with long-chain branches noticeably exceed those of conventional polyethylenes with similar molecular weights.

There are two ways to model viscoelasticity of a polymer melt. According to the first (which goes back to [20,21]), the melt is treated as a transient network of strands, and its time-dependent response is associated with rearrangement of chains in the network (separation of active strands from temporary junctions and attachment of dangling chains to the network). According to the other approach [2,3], the melt is thought of as a permanent, but non-affine network of chains. The non-affinity means that junctions between chains slide with respect to their reference positions under deformation, and the deformation gradient for sliding (plastic flow) of junctions differs from that for macro-deformation. Following the latter concept, we treat a thermoplastic-elastomer melt as an incompressible, inhomogeneous, non-affine network of chains linked by junctions (entanglements and physical cross-links). Heterogeneity of the network is induced by local density fluctuations. To account for the inhomogeneity, a melt is thought of as an ensemble of meso-regions with various activation energies for sliding. Distribution of meso-regions is assumed to be independent of temperature and mechanical factors.

Stress–strain relations for a polymer melt and kinetic equations for sliding (plastic flow) of junctions are developed by using the laws of thermodynamics. The conventional method of derivation is grounded on the assumption that the plastic vorticity tensor vanishes. A novelty of our approach is that the constitutive equations are deduced without any hypothesis regarding this tensor.

An advantage of the constitutive model is that it involves a small number of adjustable parameters (5 for an isothermal loading and 8 for arbitrary non-isothermal deformations) with transparent physical meaning. These quantities are determined by fitting the experimental data in shear tests with small and large strains. Not more than 3 constants are found by approximation of observations in each test, which ensures that material parameters are determined with a high level of accuracy. Ability of the constitutive equations to describe the mechanical response of TPE melts is ex-

amined by comparison of the model predictions with experimental data in additional start-up shear tests with relatively large strain rates.

The stress–strain relations are applied to study the Poiseuille flow of TPE melt in a channel. Analysis of the Poiseuille flow of viscoelastic fluids has attracted noticeable attention in the past two decades for this type of flow (i) allows constitutive models to be tested under a spatially inhomogeneous deformation program, and (ii) reveals a number of interesting phenomena (melt fracture, wall slip, secondary flows) whose modeling remains a subject of debate [23–26]. Poiseuille flow has been investigated in [27–29] for polymer fluids described by simple differential models in nonlinear viscoelasticity, in [30] for the Wagner model, in [31,32] for the Johnson–Segalman model, in [33–36] for the Giesekus model, in [36,37] for the Leonov model, in [38] for the Phan-Thien–Tanner model, in [39,40] for the FENE model, in [41–44] for viscoelastic-plastic fluids, and in [45] for viscoelastic fluids with pressure-dependent viscosity. We concentrate on combined effects of temperature and pressure gradient on steady velocity profile.

The objective of the present study is three-fold:

1. To report experimental data in oscillatory shear tests with small amplitudes and start-up shear tests with finite strains at various temperatures on ethylene-octene copolymer melt.

2. To derive constitutive equations in finite thermo-viscoelasticity of polymer melts and to find adjustable parameters in the stress–strain relations by fitting the observations.

3. To analyze the influence of temperature and pressure gradient on the velocity profile for Poiseuille flow of the TPE melt.

The exposition is organized as follows. Experimental data are presented in Section 2. Kinematic relations for an incompressible heterogeneous non-affine polymer network are derived in Section 3. Constitutive equations for a polymer melt are developed in Section 4 by using the laws of thermodynamics. The stress–strain relations are applied to the analysis of simple shear in Section 5. Adjustable parameters in the constitutive equations are found in Section 6 by fitting the experimental data. Ability of the model to predict observations in shear tests with large strain rates and to follow the Cox–Merz rule is examined in Section 7. The Poiseuille flow of TPE melt is studied in Section 8. Concluding remarks are formulated in Section 9.

2 Experimental procedure

Thermoplastic elastomer Engage 8101 (ethylene-octene copolymer with 31 wt.-% of comonomer) was supplied by DuPont–Dow Elastomers. Rheological tests were performed by using rheometric mechanical spectrometer Paar Physica MCR 500 in the cone–plate mode with a diameter of the disk 25 mm and 2° probe.

Two series of experiments were conducted at the temperatures T=120, 130, 150, 170, 190, and 210 °C. The lowest temperature T=120 °C was chosen from the condition

that torque in small-amplitude oscillatory tests did not exceed its critical value at the highest frequency. The highest temperature T=210 °C was chosen to ensure that no noticeable degradation of samples occurred during shear oscillatory tests with a duration of 25 min (pronounced degradation was observed in dynamic tests at $T_{\rm d}$=230 °C).

The first series involved small-amplitude shear oscillatory tests (in the frequency-sweep mode) with an amplitude of 0.05 and angular frequencies ranging from 0.1 to 100 rad/s. In an oscillatory test, a sample was equilibrated at a required temperature, and the storage modulus G' and loss modulus G'' were measured at various frequencies ω beginning from the largest one. Each test was conducted on a new sample. The experimental data are depicted in Figs. 1 and 2 in the form of the standard double-logarithmic plots with $\log=\log_{10}$.

The other series of experiments involved start-up shear tests with constant shear rates $\dot{k}$. At a given temperature, four tests were conducted with the strain rates $\dot{k}$=1, 2, 5, and 10 s^{-1}. Each tests was performed on a new specimen. The experimental data are presented in Figs. 3–8, where the shear stress Σ is plotted versus shear k. We confined ourselves to the interval $0 \leq k \leq 10$, as steady shear flow was established within this interval at all temperatures.

The following conclusion are drawn from Figs. 1–8:

1. Given a temperature T, the storage and loss moduli monotonically increase with frequency of oscillations.

2. Given an angular frequency ω, the storage and loss moduli decrease with temperature. The curves $G''(\omega)$ measured at various temperatures are practically parallel to each other, whereas shape of the curves $G'(\omega)$ changes, and the dependence $G'(\omega)$ becomes steeper at elevated temperatures.

3. Given a temperature T, the shear stress Σ in start-up tests strongly grows with shear rate.

4. Given a shear rate $\dot{k}$, the shear stress in start-up tests decreases pronouncedly with temperature.

5. When the temperature T exceeds 130 °C, the dependencies $\Sigma(k)$ are monotonous at all strain rates under consideration. At the lowest temperature T=120 °C, stress overshoot is observed at relatively high shear rates.

3 Kinematics of a non-affine network

A thermoplastic-elastomer melt is modeled as an incompressible heterogeneous non-affine polymer network, where junctions between chains slide with respect to their reference positions. The inhomogeneity of the network is induced by local density fluctuations. To account for this phenomenon, we treat the melt as an ensemble of meso-regions, where sliding (plastic flow) of junctions occurs with various rates. Each meso-region is characterized by some energy of inter-chain interaction $\bar{u}$. The rate of

sliding Γ is expressed in terms of $\bar{u}$ by means of the Eyring formula [46]

$$\Gamma = \gamma \exp\Big(-\frac{\bar{u}}{k_B T_0}\Big), \tag{3.1}$$

where T_0 stands for some reference temperature, and the pre-factor γ depends (in general) on absolute temperature T and mechanical factors. By introducing the dimensionless energy

$$u = \frac{\bar{u}}{k_B T_0},$$

we present Eq. (3.1) in the form

$$\Gamma(t,u) = \gamma(t) \exp(-u), \tag{3.2}$$

where an explicit dependence of γ on time reflects evolution of this quantity driven by deformation.

Distribution of meso-regions with various energies is determined by (i) the number $n(u)$ of chains (per unit volume) that belong to a meso-region with dimensionless energy u, and (ii) the entire number of chains per unit volume of the melt

$$n_0 = \int_0^\infty n(u) \mathrm{d}u. \tag{3.3}$$

The distribution function of chains belonging to meso-regions with various u is given by

$$f(u) = \frac{n(u)}{n_0}. \tag{3.4}$$

The function $f(u)$ and the number of chains per unit volume n_0 are assumed to be independent of deformation. Constitutive equations are derived for an arbitrary distribution function $f(u)$. To fit experimental data, we adopt the random energy model [47] with

$$f(u) = f_0 \exp\Big(-\frac{u^2}{2\sigma^2}\Big), \quad (u \geq 0), \qquad f(u) = 0, \quad (u < 0), \tag{3.5}$$

where the pre-factor f_0 is determined by the normalization condition. An advantage of Eq. (3.5) is that it involves the only material constant $\sigma > 0$.

At time $t \geq 0$, macro-deformation of the melt is characterized by the deformation gradient $\mathbf{F}(t)$, and sliding of junctions in a meso-region with energy u is described by the deformation gradient $\mathbf{F}_{\rm s}(t,u)$. The incompressibility condition implies that the third principal invariants of the tensors $\mathbf{F}(t)$ and $\mathbf{F}_{\rm s}(t,u)$ equal unity.

The velocity gradient for the sliding process $\mathbf{l}_{\rm s}(t,u)$ reads

$$\mathbf{l}_{\rm s} = \frac{\partial \mathbf{F}_{\rm s}}{\partial t} \cdot \mathbf{F}_{\rm s}^{-1}, \tag{3.6}$$

where the dot stands for inner product. The rate-of-strain tensor $\mathbf{d}_s(t,u)$ and the vorticity tensor $\mathbf{w}_s(t,u)$ for sliding of junctions are given by

$$\mathbf{d}_s = \frac{1}{2}(\mathbf{l}_s + \mathbf{l}_s^\top), \qquad \mathbf{w}_s = \frac{1}{2}(\mathbf{l}_s - \mathbf{l}_s^\top), \tag{3.7}$$

where $\top$ stands for transpose. It follows from Eq. (3.7) that

$$\mathbf{l}_s = \mathbf{d}_s + \mathbf{w}_s. \tag{3.8}$$

The deformation gradient for elastic deformation $\mathbf{F}_e(t,u)$ in a meso-region with energy u is determined by

$$\mathbf{F}_e = \mathbf{F} \cdot \mathbf{F}_s^{-1}. \tag{3.9}$$

Differentiating Eq. (3.9) with respect to time, applying Eqs. (3.6) and (3.9), and keeping in mind the formula

$$\mathbf{L} = \frac{\mathrm{d}\mathbf{F}}{\mathrm{d}t} \cdot \mathbf{F}^{-1} \tag{3.10}$$

for the velocity gradient for macro-deformation, we find that

$$\frac{\partial \mathbf{F}_e}{\partial t} = \mathbf{L}_e \cdot \mathbf{F}_e, \tag{3.11}$$

where

$$\mathbf{L}_e = \mathbf{L} - \mathbf{L}_s, \qquad \mathbf{L}_s = \mathbf{F}_e \cdot (\mathbf{d}_s + \mathbf{w}_s) \cdot \mathbf{F}_e^{-1}. \tag{3.12}$$

The rate-of-strain tensors for macro-deformation, $\mathbf{D}$, and elastic deformation, $\mathbf{D}_e$, read

$$\mathbf{D} = \frac{1}{2}(\mathbf{L} + \mathbf{L}^\top), \qquad \mathbf{D}_e = \frac{1}{2}(\mathbf{L}_e + \mathbf{L}_e^\top). \tag{3.13}$$

It follows from Eqs. (3.12) and (3.13) that

$$\mathbf{D}_e = \mathbf{D} - \mathbf{D}_s, \tag{3.14}$$

where

$$\mathbf{D}_s = \frac{1}{2}\Big(\mathbf{F}_e \cdot \mathbf{d}_s \cdot \mathbf{F}_e^{-1} + \mathbf{F}_e \cdot \mathbf{w}_s \cdot \mathbf{F}_e^{-1} + \mathbf{F}_e^{-\top} \cdot \mathbf{d}_s \cdot \mathbf{F}_e^{\top} - \mathbf{F}_e^{-\top} \cdot \mathbf{w}_s \cdot \mathbf{F}_e^{\top}|\Big). \tag{3.15}$$

The left, $\mathbf{B}_e$, and right, $\mathbf{C}_e$, Cauchy–Green tensors for elastic deformation are given by

$$\mathbf{B}_e = \mathbf{F}_e \cdot \mathbf{F}_e^{\top}, \qquad \mathbf{C}_e = \mathbf{F}_e^{\top} \cdot \mathbf{F}_e. \tag{3.16}$$

Differentiating Eq. (3.16) with respect to time and taking into account Eqs. (3.12) and (3.14), we arrive at

$$\frac{\partial \mathbf{B}_e}{\partial t} = \mathbf{L} \cdot \mathbf{B}_e + \mathbf{B}_e \cdot \mathbf{L}^\top - (\mathbf{L}_s \cdot \mathbf{B}_e + \mathbf{B}_e \cdot \mathbf{L}_s^\top), \tag{3.17}$$

$$\frac{\partial \mathbf{C}_e}{\partial t} = 2\mathbf{F}_e^{\top} \cdot \mathbf{D} \cdot \mathbf{F}_e - 2\mathbf{F}_e^{\top} \cdot \mathbf{D}_s \cdot \mathbf{F}_e. \tag{3.18}$$

It follows from Eqs. (3.12), (3.15), and (3.16) that

$$\mathbf{L}_s \cdot \mathbf{B}_e + \mathbf{B}_e \cdot \mathbf{L}_s^\top = 2\mathbf{F}_e \cdot \mathbf{d}_s \cdot \mathbf{F}_e^\top,$$
$$2\mathbf{F}_e^\top \cdot \mathbf{D}_s \cdot \mathbf{F}_e = \mathbf{C}_e \cdot \mathbf{d}_s + \mathbf{d}_s \cdot \mathbf{C}_e + \mathbf{C}_e \cdot \mathbf{w}_s - \mathbf{w}_s \cdot \mathbf{C}_e.$$

Insertion of these expressions into Eq. (3.18) results in

$$\frac{\partial \mathbf{B}_e}{\partial t} = \mathbf{L} \cdot \mathbf{B}_e + \mathbf{B}_e \cdot \mathbf{L}^\top - 2\mathbf{F}_e \cdot \mathbf{d}_s \cdot \mathbf{F}_e^\top, \tag{3.19}$$
$$\frac{\partial \mathbf{C}_e}{\partial t} = 2\mathbf{F}_e^\top \cdot \mathbf{D} \cdot \mathbf{F}_e - (\mathbf{C}_e \cdot \mathbf{d}_s + \mathbf{d}_s \cdot \mathbf{C}_e) - (\mathbf{C}_e \cdot \mathbf{w}_s - \mathbf{w}_s \cdot \mathbf{C}_e). \tag{3.20}$$

The first principal invariant of the tensor $\mathbf{C}_e$ is given by

$$J_{e1} = \mathbf{C}_e : \mathbf{I}, \tag{3.21}$$

where $\mathbf{I}$ is the unit tensor, and the colon stands for convolution. Differentiating Eq. (3.21) with respect to time, using Eq. (3.20), and bearing in mind that the tensors $\mathbf{D}$ and $\mathbf{d}_s$ are traceless, we find that

$$\frac{\partial J_{e1}}{\partial t} = 2(\mathbf{B}_e' : \mathbf{D} - \mathbf{C}_e' : \mathbf{d}_s), \tag{3.22}$$

where the prime stands for the deviator of a tensor.

4 Constitutive equations

The strain energy of a polymer chain at time t in a meso-region with dimensionless energy u is determined by the classical formula for a neo-Hookean medium

$$w(t,u) = \frac{1}{2}\tilde{\mu}\Big(J_{e1}(t,u) - 3\Big), \tag{4.1}$$

where $\tilde{\mu}$ stands for rigidity. The strain energy density per unit volume of a network $W(t)$ equals the sum of strain energies of chains belonging to meso-regions with various energies u,

$$W(t) = \int_0^\infty w(t,u) n(u) \mathrm{d}u. \tag{4.2}$$

Combination of Eqs. (4.1) and (4.2) results in

$$W(t) = \frac{1}{2}\mu \int_0^\infty \Big(J_{e1}(t,u) - 3\Big) f(u) \mathrm{d}u, \tag{4.3}$$

where we introduced the notation $\mu = \tilde{\mu} n_0$. Differentiating Eq. (4.3) with respect to time and using Eq. (3.22), we obtain

$$\frac{\mathrm{d}W}{\mathrm{d}t}(t) = \mu \left[\int_0^\infty \mathbf{B}_e'(t,u) f(u) \mathrm{d}u : \mathbf{D}(t) - \int_0^\infty \mathbf{C}_e'(t,u) : \mathbf{d}_s(t,u) f(u) \mathrm{d}u \right]. \tag{4.4}$$

At isothermal deformation of an incompressible medium, the Clausius–Duhem inequality reads

$$Q(t) = -\frac{\mathrm{d}W}{\mathrm{d}t}(t) + \mathbf{\Sigma}'(t) : \mathbf{D}(t) \geq 0, \tag{4.5}$$

where Q stands for internal dissipation per unit volume and unit time, and $\mathbf{\Sigma}$ is the Cauchy stress tensor. Substitution of expression (4.4) into Eq. (4.5) implies that

$$Q(t) = \Big[\mathbf{\Sigma}(t) - \mu \int_0^\infty \mathbf{B}_{\mathrm{e}}(t,u) f(u) \mathrm{d}u\Big]' : \mathbf{D}(t) + \mu \int_0^\infty \mathbf{C}_{\mathrm{e}}'(t,u) : \mathbf{d}_{\mathrm{s}}(t,u) f(u) \mathrm{d}u \geq 0. \tag{4.6}$$

Inequality (4.6) is satisfied for an arbitrary deformation program, provided that the stress tensor is given by

$$\mathbf{\Sigma}(t) = -p(t)\mathbf{I} + \mu \int_0^\infty \mathbf{B}_{\mathrm{e}}(t,u) f(u) \mathrm{d}u, \tag{4.7}$$

where $p(t)$ is an unknown pressure, and the rate-of strain tensor $\mathbf{d}_{\mathrm{s}}$ obeys the kinetic equation

$$\mathbf{d}_{\mathrm{s}}(t,u) = \Gamma(t,u) \mathbf{C}_{\mathrm{e}}'(t,u). \tag{4.8}$$

Eq. (4.8) may be treated as a definition of the rate of sliding of junctions Γ in a meso-region with energy u.

To rearrange Eq. (3.19) for the tensor $\mathbf{B}_{\mathrm{e}}$, we present Eq. (4.8) in the form

$$\mathbf{d}_{\mathrm{s}} = \Gamma(\mathbf{C}_{\mathrm{e}} - \frac{1}{3} J_{\mathrm{e}1} \mathbf{I}). \tag{4.9}$$

It follows from Eqs. (3.16), (3.19) and (4.9) that

$$\frac{\partial \mathbf{B}_{\mathrm{e}}}{\partial t} = \mathbf{L} \cdot \mathbf{B}_{\mathrm{e}} + \mathbf{B}_{\mathrm{e}} \cdot \mathbf{L}^{\top} - 2\Gamma(\mathbf{B}_{\mathrm{e}}^2 - \frac{1}{3} J_{\mathrm{e}1} \mathbf{B}_{\mathrm{e}}). \tag{4.10}$$

The initial condition for Eq. (4.10)

$$\mathbf{B}_{\mathrm{e}}(0,u) = \mathbf{I}, \tag{4.11}$$

means that elastic strains vanish in the reference state.

To complete description of the constitutive model, a dependence of the rate γ should be established on temperature T and intensity of elastic deformations. We postulate that

$$\gamma = \tilde{\gamma}(T) \psi(\mathbf{B}_{\mathrm{e}}), \tag{4.12}$$

where $\tilde{\gamma}$ and ψ are given functions, and adopt the Arrhenius dependence of $\tilde{\gamma}$ on temperature

$$\tilde{\gamma} = \gamma_0 \exp\Big(-\frac{E_{\mathrm{a}}}{RT}\Big), \tag{4.13}$$

where γ_0 is a constant pre-factor, E_a stands for an apparent activation energy, and R denotes the universal gas constant.

The effect of deformation of the rate of sliding is described by the formula

$$\psi = 1 - a\Big[1 - \exp\Big(-g(J_{e2} - 3)\Big)\Big], \tag{4.14}$$

where a and g are positive dimensionless constants, and J_{e2} stands for the second principal invariant of the tensor $\mathbf{B}_e$. Eq. (4.14) implies that the function ψ equals unity at infinitesimal deformations, decreases monotonically with deformation, and reaches its ultimate value $1 - a$ at large strains.

Formulas (3.2), (3.5), (4.7), and (4.10)–(4.14) provide stress–strain relations for a polymer melt. Given a temperature T, the constitutive equations involve 5 material parameters:

1. the modulus μ characterizes elastic properties of the melt,
2. the rate $\tilde{\gamma}$ describes viscoplastic flow of junctions at small strains,
3. σ reflects local heterogeneity of the polymer network,
4. a and g account for the effect of strain on flow of junctions.

To describe the effect of temperature on the mechanical response, it is postulated that in the interval of temperatures under consideration, i.e. above the melting temperature T_m and below the temperature T_d at which noticeable degradation of TPE melt occurs:

1. The dimensionless parameters a and σ are independent of temperature.
2. The elastic modulus μ linearly grows with temperature

$$\mu = \mu_0 + \mu_1 T, \tag{4.15}$$

where μ_0 and μ_1 are positive coefficients. Eq. (4.15) is in accord with the statistical theory of rubber elasticity that presumes the strain energy of a polymer chain, and, as a consequence, its elastic modulus, to be proportional to temperature.

3. The dimensionless parameter g linearly increases with temperature,

$$g = g_0 + g_1 T, \tag{4.16}$$

where g_0 and g_1 are constants.

The set of governing equations for an arbitrary non-isothermal deformation of a polymer melt involves 8 material constants $a, E_a, g_0, g_1, \gamma_0, \mu_0, \mu_1, \sigma$.

The stress–strain relations (4.7) and (4.10)–(4.14) belong to a class of multi-mode Leonov models. The following issues distinguish these equations from the Leonov model [1] and its previous modifications:

1. Within conventional multi-mode models, the relaxation spectrum of a melt is described by means of a set of characteristic relaxation times and appropriate elastic

moduli. A shortcoming of that approach is that it (i) requires a large number of adjustable parameters to be determined simultaneously by fitting observations in small-amplitude oscillatory tests, and (ii) leads to unphysical oscillations when the steady extensional viscosity is calculated as a function of elongation rate [48]. In the present model, the relaxation spectrum is determined by two adjustable parameters, γ_0 and σ, which ensures that these quantities are found with a high level of accuracy by matching observations.

2. The constitutive equations do not presume separation of the effects of temperature and material nonlinearity of the mechanical response, since Eqs. (4.10), (4.12) and (4.16) account for an increase in parameter g with temperature. The latter means that the influence of nonlinearity on the time-dependent behavior of TPE melt becomes more pronounced with growth of temperature.

3. In contradiction with traditional models, Eq. (4.14) implies that the rate of sliding of junctions decreases with elastic strains. This hypothesis is confirmed in Section 6 by comparison of results of numerical simulation with experimental data. This "anomalous" behavior of ethylene-octene copolymer melt (slowing down of the viscoplastic flow of junctions with deformation) may be attributed to interaction between long branched chains and formation of temporary physical cross-links with relatively short life-times.

5 Simple shear

Macro-deformation at simple shear of an incompressible medium is described by the equations

$$x_1 = X_1 + k(t)X_2, \qquad x_2 = X_2, \qquad x_3 = X_3, \tag{5.1}$$

where $\{X_i\}$ and $\{x_i\}$ are Cartesian coordinates in the initial and actual states, respectively, and $k(t)$ stands for shear. Eqs. (5.1) imply that

$$\mathbf{F}(t) = \mathbf{e}_1\mathbf{e}_1 + \mathbf{e}_2\mathbf{e}_2 + \mathbf{e}_3\mathbf{e}_3 + k(t)\mathbf{e}_1\mathbf{e}_2,$$

where $\mathbf{e}_m$ ($m = 1, 2, 3$) are basic vectors of the coordinate frame $\{X_m\}$. Insertion of this expression into Eq. (3.10) yields

$$\mathbf{L}(t) = \dot{k}(t)\mathbf{e}_1\mathbf{e}_2, \tag{5.2}$$

where $\dot{k} = \mathrm{d}k/\mathrm{d}t$.

We search the deformation gradient $\mathbf{F}_{\mathrm{e}}(t, u)$ in the form

$$\mathbf{F}_{\mathrm{e}} = p_1\mathbf{e}_1\mathbf{e}_1 + p_2\mathbf{e}_2\mathbf{e}_2 + p_3\mathbf{e}_3\mathbf{e}_3 + \phi\mathbf{e}_1\mathbf{e}_2, \tag{5.3}$$

where $\phi(t, u)$ and $p_m(t, u)$ ($m = 1, 2, 3$) are scalar functions to be found. These functions obey the incompressibility condition

$$p_1p_2p_3 = 1. \tag{5.4}$$

Eq. (5.3) means that elastic deformation of a melt is treated as superposition of shear and three-dimensional extension. Combination of Eqs. (3.16) and (5.3) results in

$$\mathbf{B}_{\rm e} = (p_1^2+\phi^2)\mathbf{e}_1\mathbf{e}_1 + p_2^2\mathbf{e}_2\mathbf{e}_2 + p_3^2\mathbf{e}_3\mathbf{e}_3 + p_2\phi(\mathbf{e}_1\mathbf{e}_2+\mathbf{e}_2\mathbf{e}_1). \tag{5.5}$$

Eqs. (5.4) and (5.5) imply that

$$J_{\rm e1} = p_1^2+p_2^2+p_3^2+\phi^2, \qquad J_{\rm e2} = \frac{1}{p_1^2}+\frac{1}{p_2^2}+\frac{1}{p_3^2}+p_3^2\phi^2. \tag{5.6}$$

Insertion of Eqs. (5.2), (5.5), and (5.6) into Eq. (4.10) yields

$$\frac{\partial}{\partial t}(p_1^2+\phi^2) = 2\dot{k}p_2\phi - 2\Gamma\Big[\frac{1}{3}(p_1^2+\phi^2)(2p_1^2-p_2^2-p_3^2+2\phi^2)+p_2^2\phi^2\Big], \tag{5.7a}$$

$$\frac{\partial}{\partial t}(p_2\phi) = \dot{k}p_2^2 - \frac{2}{3}\Gamma p_2\phi(2p_1^2+2p_2^2-p_3^2+2\phi^2), \tag{5.7b}$$

$$\frac{\partial}{\partial t}(p_2^2) = -\frac{2}{3}\Gamma p_2^2(-p_1^2+2p_2^2-p_3^2+2\phi^2), \tag{5.7c}$$

$$\frac{\partial}{\partial t}(p_3^2) = -\frac{2}{3}\Gamma p_3^2(-p_1^2-p_2^2+2p_3^2-\phi^2). \tag{5.7d}$$

The last two equations in Eqs. (5.7) read

$$\frac{\partial p_2}{\partial t} = -\frac{1}{3}\Gamma p_2(-p_1^2+2p_2^2-p_3^2+2\phi^2), \tag{5.8}$$

$$\frac{\partial p_3}{\partial t} = -\frac{1}{3}\Gamma p_3(-p_1^2-p_2^2+2p_3^2-\phi^2). \tag{5.9}$$

It follows from the second equation in Eqs. (5.7) and (5.8)-(5.9) that

$$\frac{\partial \phi}{\partial t} = \dot{k}p_2 - \frac{1}{3}\Gamma\phi(5p_1^2+2p_2^2-p_3^2+2\phi^2). \tag{5.10}$$

Rearrangement of the first equation in Eqs. (5.7) with the help of Eq. (5.10) yields

$$\frac{\partial p_1}{\partial t} = -\frac{1}{3}\Gamma p_1(2p_1^2-p_2^2-p_3^2-\phi^2). \tag{5.11}$$

Eqs. (5.9)–(5.11) with the initial conditions

$$\phi(0,u) = 0, \qquad p_m(0,u) = 1, \qquad (m=1,2,3), \tag{5.12}$$

determine evolution of the functions p_m and ϕ with time. In accord with Eqs. (3.2), (4.12), (4.14), and (5.6), the coefficient Γ reads

$$\Gamma = \tilde{\gamma}\psi\exp(-u), \tag{5.13a}$$

$$\psi = 1 - a\Big[1-\exp\Big(-g(p_1^{-2}+p_2^{-2}+p_3^{-2}+p_3^2\phi^2-3)\Big)\Big]. \tag{5.13b}$$

Insertion of Eq. (5.5) into Eq. (4.7) results in the formula for shear stress

$$\Sigma(t) = \mu\int_0^\infty p_2(t,u)\phi(t,u)f(u)\mathrm{d}u. \tag{5.14}$$

Eqs. (3.5) and (5.9)–(5.14) describe simple shear of a melt for an arbitrary deformation program $k(t)$.

5.1 Shear oscillations with a small amplitude

To examine the linear viscoelastic response of TPE melt, we suppose that $|k| \ll 1$ and present the functions ϕ and p_m in the form

$$\phi(t,u) = \Delta\phi(t,u), \qquad p_m(t,u) = 1 + \Delta p_m(t,u), \quad (m = 1,2,3), \tag{5.15}$$

where $|\Delta\phi| \ll 1$ and $|\Delta p_m| \ll 1$. Inserting expressions (5.15) into Eqs. (5.9)–(5.11) and (5.13a) and disregarding terms beyond the first order of smallness, we obtain

$$\frac{\partial \Delta p_1}{\partial t} = -\frac{2}{3}\tilde{\gamma}\exp(-u)(2\Delta p_1 - \Delta p_2 - \Delta p_3), \tag{5.16}$$

$$\frac{\partial \Delta p_2}{\partial t} = -\frac{2}{3}\tilde{\gamma}\exp(-u)(-\Delta p_1 + 2\Delta p_2 - \Delta p_3), \tag{5.17}$$

$$\frac{\partial \Delta p_3}{\partial t} = -\frac{2}{3}\tilde{\gamma}\exp(-u)(-\Delta p_1 - \Delta p_2 + 2\Delta p_3), \tag{5.18}$$

$$\frac{\partial \Delta\phi}{\partial t} = \dot{k} - 2\tilde{\gamma}\exp(-u)\Delta\phi, \tag{5.19}$$

With the required level of accuracy, initial conditions (5.12) read

$$\Delta p_m(0,u) = 0, \qquad \Delta\phi(0,u) = 0. \tag{5.20}$$

Solutions of linear homogeneous differential equations (5.18) with initial conditions (5.20) are given by

$$\Delta p_m(t,u) = 0 \qquad (m = 1,2,3).$$

Substituting Eq. (5.15) into Eq. (5.14) and neglecting terms beyond the first order of smallness, we find that

$$\Sigma(t) = \mu\int_0^\infty \Delta\phi(t,u)f(u)\mathrm{d}u. \tag{5.21}$$

Eqs. (5.19) and (5.21) describe the shear stress Σ as a function of time t in a shear test with small strains.

To derive explicit expressions for the storage and loss moduli of a polymer melt measured in an oscillatory test with small amplitude, we consider the deformation program

$$k(t) = k_0\exp(\imath\omega t), \tag{5.22}$$

where $\imath = \sqrt{-1}$, k_0 stands for amplitude, and ω denotes angular frequency. A steady-state solution of Eq. (5.19) is searched in the form

$$\Delta\phi(t,v) = \Delta\phi_0\exp(\imath\omega t), \tag{5.23}$$

where $\Delta\phi_0$ is an unknown coefficient. Insertion of Eqs. (5.22) and (5.23) into Eq. (5.19) results in

$$\Delta\phi_0 = \frac{k_0\imath\omega}{2\tilde{\gamma}\exp(-u) + \imath\omega}. \tag{5.24}$$

Substitution of Eqs. (5.22)–(5.24) into Eq. (5.21) implies that

$$\Sigma(t) = \mu k(t) \int_0^\infty \frac{\imath\omega}{2\tilde{\gamma}\exp(-u) + \imath\omega} f(u)\mathrm{d}u. \tag{5.25}$$

Introducing the notation

$$\frac{\Sigma}{k} = G'(\omega) + \imath G''(\omega),$$

where G' and G'' stand for storage and loss moduli, we find from Eq. (5.25) that

$$G'(\omega) = \mu \int_0^\infty \frac{\omega^2}{4\tilde{\gamma}^2\exp(-2u) + \omega^2} f(u)\mathrm{d}u, \tag{5.26}$$

$$G''(\omega) = \mu \int_0^\infty \frac{2\tilde{\gamma}\omega\exp(-u)}{4\tilde{\gamma}^2\exp(-2u) + \omega^2} f(u)\mathrm{d}u. \tag{5.27}$$

Eqs. (5.26) and (5.27) describe the storage, G', and loss, G'', moduli as functions of frequency of oscillations ω.

5.2 Steady shear flow with a constant strain rate

We proceed with the study of simple shear with a constant strain rate and determine the steady shear viscosity η as a function of shear rate $\dot{k}$. Assuming the functions $p_m(t)$ ($m = 1, 2, 3$), $\phi(t)$ and $\psi(t)$ to approach their limiting values p_{m0}, ϕ_0 and ψ_0 as time tends to infinity, we find from Eqs. (5.9)–(5.11) and (5.13a) that the quantities p_{m0}, ϕ_0 and ψ_0 obey the nonlinear equations

$$2p_{10}^2 - p_{20}^2 - p_{30}^2 - \phi_0^2 = 0, \tag{5.28a}$$

$$-p_{10}^2 + 2p_{20}^2 - p_{30}^2 + 2\phi_0^2 = 0, \tag{5.28b}$$

$$-p_{10}^2 - p_{20}^2 + 2p_{30}^2 - \phi_0^2 = 0, \tag{5.28c}$$

$$(5p_{10}^2 + 2p_{20}^2 - p_{30}^2 + 2\phi_0^2)\phi_0 = \frac{3\dot{k}}{\tilde{\gamma}\psi_0} p_{20}\exp(u), \tag{5.28d}$$

$$\psi_0 = 1 - a\Big[1 - \exp\Big(-g(p_{10}^{-2} + p_{20}^{-2} + p_{30}^{-2} + p_{30}^2\phi_0^2 - 3)\Big)\Big]. \tag{5.28e}$$

Subtracting the third equality in Eq. (5.28) from the first, we obtain

$$p_{30}^2 = p_{10}^2. \tag{5.29}$$

Substitution of Eq. (5.29) into the second equality in Eq. (5.28) results in

$$p_{10}^2 = p_{20}^2 + \phi_0^2. \tag{5.30}$$

Combination of Eqs. (5.4), (5.29), and (5.30) yields

$$p_{20}^2 + \phi_0^2 = \frac{1}{p_{20}}. \tag{5.31}$$

It follows from Eqs. (5.29)–(5.31) that

$$\frac{1}{p_{10}^2}+\frac{1}{p_{20}^2}+\frac{1}{p_{30}^2}+p_{30}^2\phi_0^2=p_{20}+\frac{2}{p_{20}^2}. \tag{5.32}$$

Substituting Eq. (5.32) into the last equality in Eq. (5.28), we find that

$$\psi_0(p_{20})=1-a+a\exp\Big[-g\Big(p_{20}+2p_{20}^{-2}-3\Big)\Big]. \tag{5.33}$$

Combination of Eqs. (5.29)–(5.31) with the fourth equation in Eq. (5.28) implies that

$$\phi_0=K\frac{p_{20}^2}{\psi_0}, \tag{5.34}$$

where

$$K=\frac{\dot{k}\exp(u)}{2\tilde{\gamma}}. \tag{5.35}$$

Insertion of Eq. (5.34) into Eq. (5.31) results in the nonlinear algebraic equation for p_{20},

$$p_{20}^3+\frac{K^2}{\psi_0^2}p_{20}^5-1=0. \tag{5.36}$$

It follows from Eqs. (5.14) and (5.34) that the steady shear stress Σ_0 reads

$$\Sigma_0=\mu\int_0^\infty K(u)\frac{p_{20}^3(u)}{\psi_0(p_{20}(u))}f(u)\mathrm{d}u. \tag{5.37}$$

The steady shear viscosity is defined as

$$\eta=\frac{\Sigma_0}{\dot{k}}.$$

Substituting Eq. (5.37) into this equation and using Eq. (5.35), we arrive at

$$\eta=\frac{\mu}{2\tilde{\gamma}}\int_0^\infty\frac{p_{20}^3(u)}{\psi_0(p_{20}(u))}\exp(u)f(u)\mathrm{d}u. \tag{5.38}$$

Eqs. (5.33), (5.35), (5.36) and (5.38) determine the steady shear viscosity η as a function of shear rate $\dot{k}$.

6 Fitting of observations

Adjustable parameters in the constitutive equations are found by fitting the experimental data reported in Section 2 with the help of the following algorithm.

6.1 Small-amplitude shear oscillatory tests

Each set of data depicted in Figs. 1 and 2 (for the shear modulus $G'(\omega)$ and the loss modulus $G''(\omega)$ at a given temperature T) is matched separately.

To determine the best-fit parameters μ, $\tilde{\gamma}$ and σ, we begin with approximation of the experimental data at the temperature T=130 °C. We fix some intervals $[0,\gamma_{\max}]$ and $[0,\sigma_{\max}]$, where the quantities $\tilde{\gamma}$ and σ are assumed to be located, and divide these intervals into J=10 subintervals by the points $\gamma^{(i)}=i\Delta\gamma$ and $\sigma^{(j)}=j\Delta\sigma$ ($i,j=1,\ldots,J-1$) with $\Delta\gamma=\gamma_{\max}/J$ and $\Delta\sigma=\sigma_{\max}/J$. For each pair $\{\gamma^{(i)},\sigma^{(j)}\}$, the integrals in Eq. (5.27) are evaluated numerically by the Simpson method with N=400 points and the step $\Delta v=3.5\cdot 10^{-2}$. The modulus μ is found by the least-squares technique from the condition of minimum of the function

$$H=\sum_m\Big[\log G'_{\rm exp}(\omega_m)-\log G'_{\rm num}(\omega_m)\Big]^2+\Big[\log G''_{\rm exp}(\omega_m)-\log G''_{\rm num}(\omega_m)\Big]^2,$$

where the sum is calculated over all frequencies ω_m at which the experimental data are reported, $G'_{\rm exp}$ and $G''_{\rm exp}$ are the dynamic moduli measured in a test, and $G'_{\rm num}$ and $G''_{\rm num}$ are given by Eq. (5.27). After finding the best-fit values $\gamma^{(i)}$ and $\sigma^{(j)}$, this procedure is repeated twice for the new intervals $[\gamma^{(i-1)},\gamma^{(i+1)}]$ and $[\sigma^{(j-1)},\sigma^{(j+1)}]$, to ensure an acceptable accuracy of fitting.

When the best-fit value of σ is found (it is reported in Table 1), we fix this parameter and approximate observations at other temperatures by means of the above algorithm with two adjustable constants, μ and $\tilde{\gamma}$, only. Figs. 1 and 2 demonstrate excellent agreement between the experimental data and the results of numerical simulation.

After determination of modulus μ at each temperature T separately, the dependence $\mu(T)$ is plotted in Fig. 9. The experimental data are matched by Eq. (4.15), where the coefficients μ_0 and μ_1 are found by the least-squares technique (these parameters are collected in Table 1). Fig. 9 shows that Eq. (4.15) correctly approximates

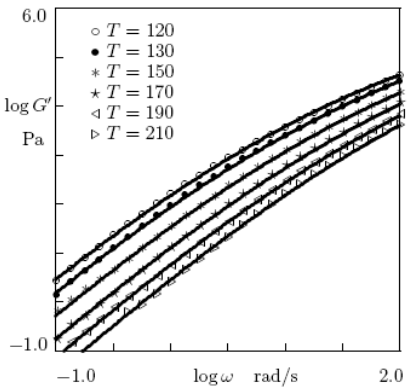

Figure 1: Storage modulus G' versus frequency ω. Symbols: experimental data on TPE melt at various temperatures T °C. Solid lines: results of numerical simulation.

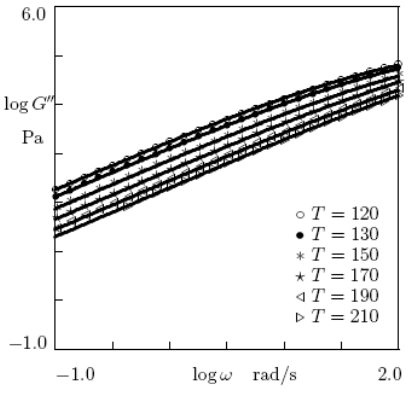

Figure 2: Loss modulus G'' versus frequency ω. Symbols: experimental data on TPE melt at various temperatures T °C. Solid lines: results of numerical simulation.

Table 1: Adjustable parameters for thermoplastic elastomer.

Parameter	Unit	Value
μ_0	kPa	$2.61 \cdot 10^{-1}$
μ_1	kPa/K	$1.08 \cdot 10^{-3}$
E_a	kJ/mol	43.02
γ_0	s^{-1}	$9.61 \cdot 10^{8}$
σ		2.10
a		0.91
g_0		$-6.99 \cdot 10^{-1}$
g_1		$6.30 \cdot 10^{-3}$

the observations. The modulus μ linearly increases with temperature, and its values belong to the interval between 0.4 and 0.5 MPa at all temperatures under consideration. This interval is close to the interval between 0.42 and 0.72 MPa which was calculated for the ultimate elastic modulus of an ethylene-octene copolymer with a similar molecular weight (at $T = 190$ °C) based on various approaches to the assessment of elastic moduli [16].

The dependence of $\tilde{\gamma}$ on temperature T is depicted in Fig. 10. The data are fitted by Eq. (4.13), which is presented in the form

$$\ln \tilde{\gamma} = c_0 - \frac{c_1}{RT}, \tag{6.1}$$

with

$$c_0 = \ln \gamma_0, \quad \text{and} \quad \mathrm{c_1} = \frac{\mathrm{E_a}}{\mathrm{R}}.$$

The coefficients c_0 and c_1 in Eq. (6.1) are calculated by the least-squares method. Fig. 10 reveals good agreement between the experimental data and their description by Eq. (6.1) with the parameters E_a and γ_0 listed in Table 1. The apparent activation energy E_a=43 kJ/mol is in accord with the observations reported by other researchers (29–39 [18], 35–36 [11], 37 [15], 39 [19], 44–45 [10] kJ/mol).

6.2 Start-up shear tests with large strains

We now fit observations in start-up shear tests with various strain rates $\dot{k}$ reported in Figs. 3–8. First, we match the experimental data in shear test with the maximum strain rate $\dot{k}$=10 s^{-1} at T=130 °C by using the parameters μ, $\tilde{\gamma}$ and σ found in the approximation of observations in small-amplitude oscillatory tests. To determine a and g, we fix some intervals $[0, a_{\max}]$ and $[0, g_{\max}]$, where these quantities are assumed to be located, and divide these intervals into J=10 subintervals by the points

$$a^{(i)} = i\Delta a, \quad \text{and} \quad g^{(j)} = j\Delta g, \quad (i, j = 1, \ldots, J-1),$$

with $\Delta a = a_{\max}/J$, and $\Delta g = g_{\max}/J$. For each pair $\{a^{(i)}, g^{(j)}\}$, Eqs. (5.9)–(5.11) with initial conditions (5.12) are integrated by the Runge–Kutta method with the step

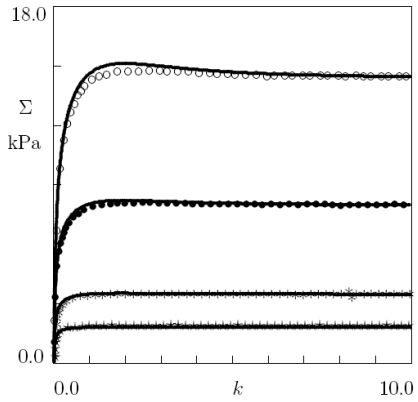

Figure 3: Shear stress Σ versus shear k in start-up tests with various strain rates $\dot{k}$ s^{-1}. Symbols: experimental data on TPE melt at the temperature $T = 120\,^{\circ}$C (unfilled circles: $\dot{k} = 10.0$, filled circles: $\dot{k} = 5.0$, asterisks: $\dot{k} = 2.0$, stars: $\dot{k} = 1.0$). Solid lines: results of numerical simulation.

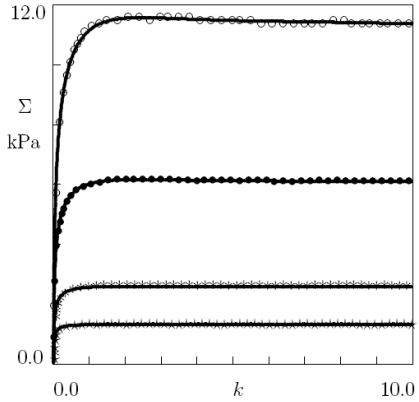

Figure 4: Shear stress Σ versus shear k in start-up tests with various strain rates $\dot{k}$ s^{-1}. Symbols: experimental data on TPE melt at the temperature $T = 130\,^{\circ}$C (unfilled circles: $\dot{k} = 10.0$, filled circles: $\dot{k} = 5.0$, asterisks: $\dot{k} = 2.0$, stars: $\dot{k} = 1.0$). Solid lines: results of numerical simulation.

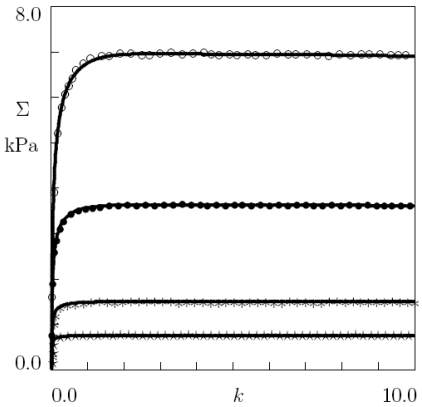

Figure 5: Shear stress Σ versus shear k in start-up tests with various strain rates $\dot{k}$ s^{-1}. Symbols: experimental data on TPE melt at the temperature $T = 150\,^{\circ}$C (unfilled circles: $\dot{k} = 10.0$, filled circles: $\dot{k} = 5.0$, asterisks: $\dot{k} = 2.0$, stars: $\dot{k} = 1.0$). Solid lines: results of numerical simulation.

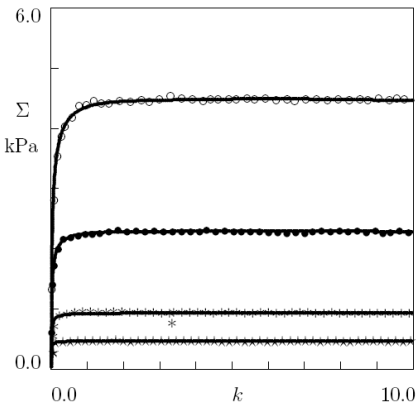

Figure 6: Shear stress Σ versus shear k in start-up tests with various strain rates $\dot{k}$ s^{-1}. Symbols: experimental data on TPE melt at the temperature $T = 170\,^{\circ}$C (unfilled circles: $\dot{k} = 10.0$, filled circles: $\dot{k} = 5.0$, asterisks: $\dot{k} = 2.0$, stars: $\dot{k} = 1.0$). Solid lines: results of numerical simulation.

Δt=$1.0 \cdot 10^{-5}$ s^{-1} for any u=$n\Delta u$ with

$$\Delta u = 3.5 \cdot 10^{-2}, \quad n = 0, 1, \ldots, N-1,$$

and N=400. The integral in Eq. (5.14) is evaluated numerically by the Simpson method. The best-fit values $a^{(i)}$ and $g^{(j)}$ are determined from the condition of minimum of the function

$$H = \sum_m \Big[\Sigma_{\rm exp}(t_m) - \Sigma_{\rm num}(t_m)\Big]^2,$$

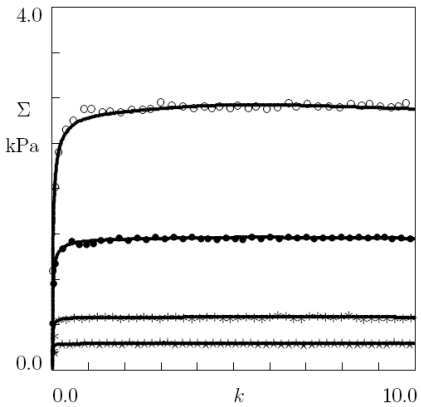

Figure 7: Shear stress Σ versus shear k in start-up tests with various strain rates $\dot{k}$ s^{-1}. Symbols: experimental data on TPE melt at the temperature $T = 190$ °C (unfilled circles: $\dot{k} = 10.0$, filled circles: $\dot{k} = 5.0$, asterisks: $\dot{k} = 2.0$, stars: $\dot{k} = 1.0$). Solid lines: results of numerical simulation.

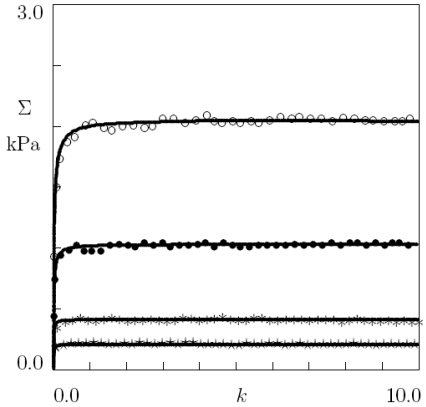

Figure 8: Shear stress Σ versus shear k in start-up tests with various strain rates $\dot{k}$ s^{-1}. Symbols: experimental data on TPE melt at the temperature $T = 210$ °C (unfilled circles: $\dot{k} = 10.0$, filled circles: $\dot{k} = 5.0$, asterisks: $\dot{k} = 2.0$, stars: $\dot{k} = 1.0$). Solid lines: results of numerical simulation.

where the sum is calculated over all instants t_m at which the experimental data are reported, $\Sigma_{\rm exp}$ is the shear stress measured in a test, and $\Sigma_{\rm num}$ is given by Eq. (5.14). After finding the best-fit values $a^{(i)}$ and $g^{(j)}$, this procedure is repeated twice for the new intervals $[a^{(i-1)}, a^{(i+1)}]$ and $[g^{(j-1)}, g^{(j+1)}]$, to ensure an acceptable accuracy of fitting.

Afterwards, we fix the best-fit value of a (it is given in Table 1) and repeat the above procedure of matching observations (in transient shear tests with the strain rate $\dot{k}$=10 s^{-1}) at other temperatures with the only adjustable parameter g.

The dependence of g on temperature T is depicted in Fig. 9. The experimental data are approximated by Eq. (4.16), where the coefficients g_0 and g_1 are found by the least-squares technique (these parameters are collected in Table 1). Fig. 9 shows that phenomenological Eq. (4.16) correctly describes the observations.

When all material parameters are found, numerical simulation of Eqs. (5.9)–(5.11) and (5.14) is performed for all temperatures T and strain rates $\dot{k}$ under consideration. The results of numerical analysis are depicted in Figs. 3–8, which reveal good agreement between the experimental data and predictions of the model.

7 Validation of the model

To validate the constitutive equations, we examine their ability (i) to predict the mechanical response in start-up shear tests with relatively high strain rates $\dot{k}$, and (ii) to describe the steady shear viscosity η as a function of strain rate $\dot{k}$. In the latter case, results of numerical simulation are compared with predictions based on the Cox–Merz rule [49].

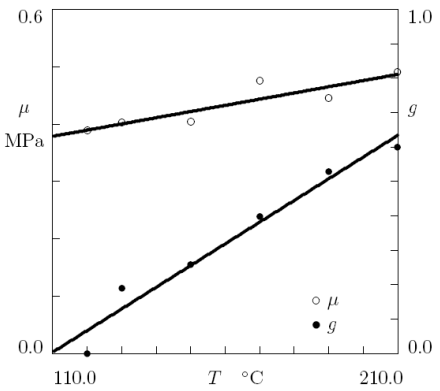

Figure 9: Modulus μ and dimensionless parameter g versus temperature T. Symbols: treatment of observations on TPE melt. Solid lines: results of numerical simulation.

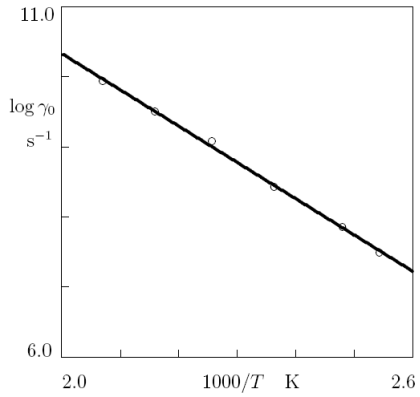

Figure 10: Rate γ_0 versus temperature T. Circles: treatment of observations on TPE melt. Solid line: results of numerical simulation.

7.1 Start-up shear tests

To check accuracy of predictions of the shear stress Σ in transient tests with large shear rates $\dot{k}$ based on constitutive equations (3.5) and (5.9)–(5.14), two additional series of experiments were conducted. The first series involved three start-up shear tests with the strain rates $\dot{k}$=40, 50 and 60 s^{-1} at the temperature T=150 °C. The other series consisted of four shear tests with the strain rate $\dot{k}$=50 s^{-1} at the temperatures T=150, 170, 190, and 210 °C. The experimental dependencies of the shear stress Σ on shear k are plotted in Figs. 11 and 12. It is worth noting that the interval of shear k in these figures substantially exceeds that in Figs. 3–8.

Afterwards, numerical simulation is performed of Eqs. (3.5) and (5.9)–(5.14) with

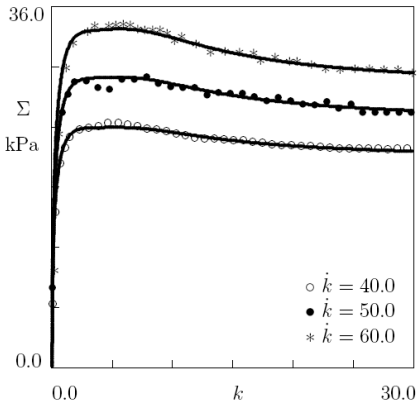

Figure 11: Shear stress Σ versus shear k in start-up tests with various strain rates $\dot{k}$ s^{-1}. Symbols: experimental data at the temperature $T = 150$ °C. Solid lines: results of numerical simulation.

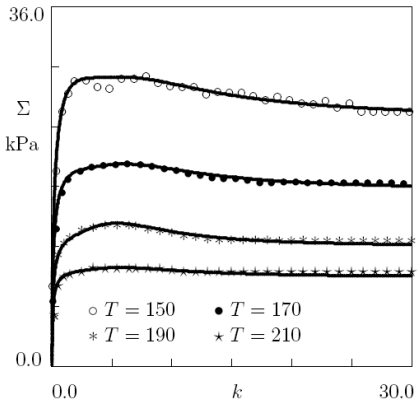

Figure 12: Shear stress Σ versus shear k in start-up tests with the strain rate $\dot{k} = 50$ s^{-1}. Symbols: experimental data at various temperatures T °C. Solid lines: results of numerical simulation.

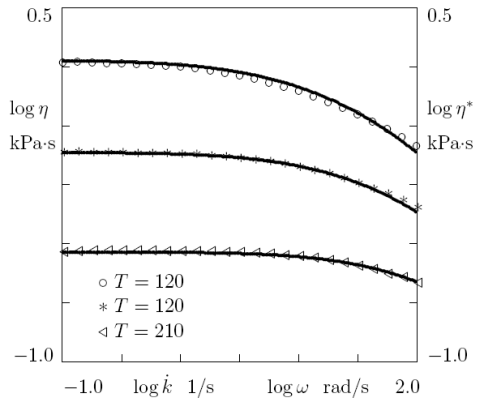

Figure 13: Shear viscosity η versus shear rate $\dot{k}$ and complex viscosity η^* versus angular frequency ω. Symbols: observations in small-amplitude oscillatory tests on TPE melt at various temperatures T °C. Solid lines: results of numerical simulation.

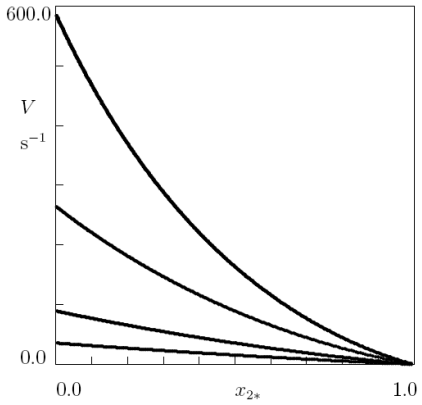

Figure 14: Velocity gradient V versus dimensionless coordinate x_{2*}. Solid lines: results of numerical simulation for steady Poiseuille flow at $T = 150$ °C with $\Delta P_* = 20$, 40, 80, and 120 kPa, from bottom to top, respectively.

the experimental constants listed in Table 1. The results of numerical analysis are also depicted in Figs. 11 and 12. These figures demonstrate good agreement between the observations and the results of simulation, which confirms that the constitutive model adequately predicts the mechanical response of TPE melt.

7.2 The Cox–Merz rule

The Cox–Merz rule states that the dependence of the complex viscosity

$$\eta^* = \frac{1}{\omega}\sqrt{(G')^2 + (G'')^2}, \tag{7.1}$$

on frequency ω in oscillatory shear tests with small amplitudes practically coincides with the dependence of the steady shear viscosity η on shear rate $\dot{k}$ in shear tests with large strains, when ω and $\dot{k}$ are measured in rad/s and s^{-1}, respectively. Although this assertion has no rigorous proof, it is fulfilled for a number of polymer melts with a high level of accuracy.

To evaluate applicability of the Cox–Merz rule to TPE melt, we calculate the dependence $\eta^*(\omega)$ by means of Eq. (7.1) and the experimental data for G' and G'' depicted in Figs. 1 and 2. Observations at the temperatures T=120, 150 and 190 °C are presented in Fig. 13.

Afterwards, the dependence of steady shear viscosity η on shear rate $\dot{k}$ is determined numerically with the help of Eqs. (5.33), (5.35), (5.36) and (5.38). Calculations are performed with the material parameters listed in Table 1. The integral in Eq. (5.38) is evaluated by the Simpson method with N=400 points and the step Δu=$3.5 \cdot 10^{-2}$. For each u, the quantity $p_{20}(u)$ is found from Eq. (5.36), which is solved by the Newton–Raphson iterative method with the minimum accuracy of $1.0 \cdot 10^{-11}$. The

results of numerical simulation are depicted in Fig. 13 which reveals that for all temperatures and frequencies (shear rates) under consideration, the response of TPE melt follows the Cox–Merz rule. At T=150 and 190 °C, the steady shear viscosity η practically coincides with the dynamic viscosity η^*, whereas at the lowest temperature T=120 °C, rather small deviations are observed between them.

8 Poiseuille flow in a channel

The constitutive model is now applied to investigate the Poiseuille flow of TPE melt in a channel with rectangular cross-section under a pressure gradient ΔP depending on time t only. We concentrate on the classical statement of the problem and disregard wall slip and flow instabilities.

The choice of the Poiseuille flow for the analysis is explained by two reasons: (i) this is the only spatially inhomogeneous motion, for which exact solutions of nonlinear constitutive equations may be developed and examined by comparison with observations of extensional viscosity [49], and (ii) explicit solutions for the Poiseuille flow of viscoelastic and viscoplastic fluids are widely used in biomedical engineering (arterial blood flow [50]) and microfluidics [51].

In a conventional microfluidic devise, when a polymer liquid moves through a micro- or nano-sized channel with rough walls (surface roughness is comparable with a characteristic width of the channel) under the action of a relatively high pressure gradient, slippage occurs at the walls that results in friction-driven dissipation of energy, part of which causes a noticeable growth of temperature [52, 53]. The increase in temperature of the liquid affects its mechanical behavior, in particular, the velocity profile, and, as a consequence, leads to changes in appropriate boundary conditions [54]. In general, a coupled thermo-mechanical problem of viscoelastic flow in a channel with nonlinear stick-slip conditions at the walls [55, 56] should be considered, which is overly complicated to expect an analytical solution to be developed. Results of numerical simulation of this problem [57, 58] are, however, rather limited because the number of material parameters is too large in order to assess the influence of various factors, on the one hand, and the physics of surface interactions is not fully understood, on the other [59]. It seems natural, as a first approximation, to decouple the entire problem and to study slippage-induced heating of a polymer fluid (with simplified motion equations) and Poiseuille flow of a viscoelastic fluid at various temperatures (with simplified boundary conditions at the walls) separately. Heat transfer in a flow of viscous fluid in a channel with rough walls has recently been investigated in [58]. Our aim is to evaluate the effects of temperature and material nonlinearities on the velocity profile for the Poiseuille flow of a TPE melt when slippage along the walls is disregarded. To the best of our knowledge, the influence of these factors on flow of polymer melts has not yet been analyzed.

The channel occupies the infinite domain

$$\{-\infty < x_1 < \infty, \quad 0 < x_2 < 2L, \quad -\infty < x_3 < \infty\},$$

where x_m ($m = 1, 2, 3$) are Cartesian coordinates with basic vectors $\mathbf{e}_m$, and $2L$ stands for width of the channel. Flow of the melt occurs in the x_1 direction, and the velocity vector $\mathbf{v}$ reads

$$\mathbf{v} = v(t, x_2)\mathbf{e}_1, \tag{8.1}$$

where $v(t, x_2)$ is a function to be found. This function obeys the no-slip boundary conditions at the walls $x_2 = 0$ and $x_2 = 2L$,

$$v(t, 0) = 0, \qquad v(t, 2L) = 0. \tag{8.2}$$

For a discussion of more realistic boundary conditions induced by wall slip, see [55, 56, 59–61]. Assuming the flow to be symmetric with respect to the plane $x_2 = L$, we replace Eq. (8.2) with

$$v(t, 0) = 0, \qquad V(t, L) = 0, \tag{8.3}$$

where

$$V = \frac{\partial v}{\partial x_2}. \tag{8.4}$$

8.1 Constitutive equations

As flow of TPE melt is studied in the reference coordinate frame, some modifications of the stress–strain relations are to be performed. First, we re-write Eq. (4.7) in the form

$$\mathbf{\Sigma} = -p\mathbf{I} + \mathbf{T}, \tag{8.5}$$

where p denotes pressure, and

$$\mathbf{T} = \mu \int_0^\infty \Big(\mathbf{B}_{\rm e} - \frac{1}{3} J_{\rm e1} \mathbf{I} \Big) f(u) \mathrm{d}u \tag{8.6}$$

stands for the traceless extra-stress tensor. Secondly, we replace the partial derivative with respect to time in Eq. (4.10) with the substantial derivative

$$\frac{\mathrm{D}}{\mathrm{D}t} = \frac{\partial}{\partial t} + \mathbf{v} \cdot \nabla, \tag{8.7}$$

which results in the kinetic equation for the left Cauchy–Green tensor for elastic deformation

$$\frac{\mathrm{D}\mathbf{B}_{\rm e}}{\mathrm{D}t} = \mathbf{L} \cdot \mathbf{B}_{\rm e} + \mathbf{B}_{\rm e} \cdot \mathbf{L}^\top - 2\Gamma(\mathbf{B}_{\rm e}^2 - \frac{1}{3} J_{\rm e1} \mathbf{B}_{\rm e}). \tag{8.8}$$

The Cauchy–Green tensor $\mathbf{B}_{\rm e}$ is presumed to depend on time, dimensionless energy u, and coordinate x_2 only,

$$\mathbf{B}_{\rm e} = \mathbf{B}_{\rm e}(t, x_2, u). \tag{8.9}$$

Under conditions (8.1) and (8.9), we have

$$\mathbf{v} \cdot \nabla \mathbf{B}_{\rm e} = v \mathbf{e}_1 \cdot \mathbf{e}_2 \frac{\partial \mathbf{B}_{\rm e}}{\partial x_2} = 0,$$

which implies that for this type of flow, substantial derivative (8.7) of the tensor $\mathbf{B}_e$ coincides with its partial derivative with respect to time,

$$\frac{D\mathbf{B}_e}{Dt} = \frac{\partial \mathbf{B}_e}{\partial t}. \tag{8.10}$$

The velocity gradient for macro-deformation reads

$$\mathbf{L} = (\nabla \mathbf{v})^\top.$$

Insertion of Eq. (8.1) into this relation implies that

$$\mathbf{L} = V \mathbf{e}_1 \mathbf{e}_2. \tag{8.11}$$

We search the tensor $\mathbf{B}_e$ in the form (5.5), where $p_m(t, x_2, u)$ $(m = 1, 2, 3)$ and $\phi(t, x_2, u)$ are functions to be found. Substitution of Eqs. (5.5), (8.10), and (8.11) into Eq. (8.8) results in the differential equations

$$\frac{\partial p_1}{\partial t} = -\frac{1}{3}\Gamma p_1(2p_1^2 - p_2^2 - p_3^2 - \phi^2), \tag{8.12a}$$

$$\frac{\partial p_2}{\partial t} = -\frac{1}{3}\Gamma p_2(-p_1^2 + 2p_2^2 - p_3^2 + 2\phi^2), \tag{8.12b}$$

$$\frac{\partial p_3}{\partial t} = -\frac{1}{3}\Gamma p_3(-p_1^2 - p_2^2 + 2p_3^2 - \phi^2), \tag{8.12c}$$

$$\frac{\partial \phi}{\partial t} = V p_2 - \frac{1}{3}\Gamma \phi(5p_1^2 + 2p_2^2 - p_3^2 + 2\phi^2). \tag{8.12d}$$

Eqs. (8.12) coincide with Eqs. (5.9)–(5.11), where the shear rate $\dot{k}$ is replaced with V.

It follows from Eqs. (8.6) and (8.9) that the extra-stress tensor $\mathbf{T}$ depends on time and coordinate x_2 only,

$$\mathbf{T} = \mathbf{T}(t, x_2). \tag{8.13}$$

Insertion of Eqs. (5.5) and (5.6) into Eq. (8.6) yields

$$\mathbf{T} = T_{11}\mathbf{e}_1\mathbf{e}_1 + T_{22}\mathbf{e}_2\mathbf{e}_2 + T_{33}\mathbf{e}_3\mathbf{e}_3 + T(\mathbf{e}_1\mathbf{e}_2 + \mathbf{e}_2\mathbf{e}_1), \tag{8.14}$$

where

$$T_{11} = \frac{\mu}{3}\int_0^\infty (2p_1^2 - p_2^2 - p_3^2 + 2\phi^2) f(u) \mathrm{d}u, \tag{8.15a}$$

$$T_{22} = \frac{\mu}{3}\int_0^\infty (-p_1^2 + 2p_2^2 - p_3^2 - \phi^2) f(u) \mathrm{d}u, \tag{8.15b}$$

$$T_{33} = \frac{\mu}{3}\int_0^\infty (-p_1^2 - p_2^2 + 2p_3^2 - \phi^2) f(u) \mathrm{d}u, \tag{8.15c}$$

$$T = \mu \int_0^\infty p_2 \phi f(u) \mathrm{d}u. \tag{8.15d}$$

8.2 Governing equations

We treat pressure p as a function of time and Cartesian coordinates, $p = p(t, x_1, x_2, x_3)$. This function is connected with the pressure gradient ΔP by the formula

$$\frac{\partial p}{\partial x_1} = -\Delta P. \tag{8.16}$$

The momentum equation for a polymer melt reads

$$\rho \frac{\mathrm{D}\mathbf{v}}{\mathrm{D}t} = -\nabla p + \nabla \cdot \mathbf{T}, \tag{8.17}$$

where ρ stands for a constant mass density. Bearing in mind that

$$\frac{\partial \mathbf{v}}{\partial t} = \frac{\partial v}{\partial t}\mathbf{e}_1, \qquad \mathbf{v} \cdot \nabla \mathbf{v} = 0, \qquad \nabla \cdot \mathbf{T} = \frac{\partial T}{\partial x_2}\mathbf{e}_1 + \frac{\partial T_{22}}{\partial x_2}\mathbf{e}_2,$$

and using Eq. (8.7), we present Eq. (8.17) in the form

$$\rho \frac{\partial v}{\partial t} = -\frac{\partial p}{\partial x_1} + \frac{\partial T}{\partial x_2}, \qquad 0 = -\frac{\partial p}{\partial x_2} + \frac{\partial T_{22}}{\partial x_2}, \qquad 0 = -\frac{\partial p}{\partial x_3}. \tag{8.18}$$

Insertion of Eqs. (8.15) and (8.16) into the first equality in Eq. (8.18) results in

$$\rho \frac{\partial v}{\partial t} = \Delta P + \mu \frac{\partial}{\partial x_2} \int_0^\infty p_2 \phi f(u) \mathrm{d}u. \tag{8.19}$$

Formulas (8.4), (8.12) and (8.19) provide a set of integro-differential equations for the unknown velocity v.

8.3 Steady-state flow of a melt

We focus on a steady-state solution of the governing equations with a constant pressure gradient ΔP, when the dependence of unknown functions on time is disregarded. It follows from Eq. (8.19) that

$$\frac{\partial}{\partial x_2} \int_0^\infty p_2 \phi f(u) \mathrm{d}u = -\frac{\Delta P}{\mu}, \tag{8.20}$$

where the same notation is preserved for the steady-state values of unknown functions. The steady-state solution of Eq. (8.12) satisfies nonlinear algebraic equations (5.28), where $\dot{k}$ is replaced with V. By analogy with Eqs. (5.33)–(5.36), we infer that the function p_2 obeys the equation

$$p_2^3 + \frac{K^2}{\psi^2} p_2^5 - 1 = 0, \tag{8.21}$$

and the function ϕ is given by

$$\phi = K\frac{p_2^2}{\psi(p_2)}, \tag{8.22}$$

where

$$K = \frac{V\exp(u)}{2\tilde{\gamma}}, \qquad \psi(p_2) = 1 - a + a\exp\Big[-g\Big(p_2 + 2p_2^{-2} - 3\Big)\Big]. \tag{8.23}$$

Eqs. (8.21) and (8.22) imply that

$$p_2\Big|_{V=0} = 1, \qquad \phi\Big|_{V=0} = 0. \tag{8.24}$$

Integration of Eq. (8.20) from x_2 to L results in

$$\int_0^\infty p_2\phi f(u)\mathrm{d}u\Big|_{x_2=L} - \int_0^\infty p_2\phi f(u)\mathrm{d}u\Big|_{x_2=x_2} = -\frac{\Delta P}{\mu}(L - x_2).$$

Keeping in mind the last boundary condition (8.3) and Eqs. (8.23) and (8.24), we obtain

$$\int_0^\infty K\frac{p_2^3}{\psi(p_2)}f(u)\mathrm{d}u = \frac{\Delta P}{\mu}(L - x_2). \tag{8.25}$$

Eqs. (8.21)–(8.23) and (8.25) provide a set of nonlinear equations for the function $V(x_2)$. When this function is found, the steady-state velocity $v(x_2)$ is determined by integration of Eq. (8.4) with the first boundary condition (8.3).

To reduce the number of parameters that describe the Poiseuille flow, on the one hand, and to preserve the structure of governing equations, on the other, we introduce the variables

$$x_{2*} = \frac{x_2}{L}, \qquad v_* = \frac{v}{L}, \qquad \Delta P_* = L\Delta P.$$

In the new notation, Eqs. (8.21)–(8.23) remain unchanged, whereas Eq. (8.25) reads

$$\int_0^\infty K\frac{p_2^3}{\psi(p_2)}f(u)\mathrm{d}u = \Delta P_*(1 - x_{2*}). \tag{8.26}$$

The steady-state velocity v_* is given by

$$v_*(x_{2*}) = \int_0^{x_{2*}} V(z)\mathrm{d}z. \tag{8.27}$$

8.4 Numerical simulation

To evaluate the effect of temperature T on velocity v, numerical simulation is performed of Eqs. (8.21)–(8.23), (8.26), and (8.27) with the material parameters listed in Table 1. Given temperature T and pressure gradient ΔP_*, we fix some value V, and find a solution p_2 of Eqs. (8.21)–(8.23). For any $u{=}n\Delta u$ with $\Delta u{=}3.5\cdot 10^{-2}$,

$n = 0, 1, \ldots, N-1$, and N=400, this solution is determined by the Newton–Raphson iterative algorithm with the accuracy of $1.0 \cdot 10^{-11}$. When the dependence $p_2(u)$ is found for a given V, the integral in Eq. (8.26) is evaluated by the Simpson method, and the dimensionless coordinate x_{2*} is calculated. Inverting the dependence $x_{2*}(V)$, the velocity gradient V is found as a function of x_{2*}. In accord with Eq. (8.27), upon integration of this function, $v_*(x_{2*})$ is determined. Calculations are carried out for V=$i\Delta V$ with the step ΔV=0.03, $i = 1, 2, \ldots, I$, and I=10^5.

The dependencies $V(x_{2*})$ and $v_*(x_{2*})$ are presented in Figs. 14 and 15 (for T=150 °C) and 16 and 17 (for T=210 °C). Results of numerical analysis are reported for various values of ΔP_* ranging from 20 to 120 kPa (which roughly correspond to the dimensionless ratios $\Delta P_*/\mu$ in the interval between 0.05 and 0.3). Figs. 14 and 16 demon-

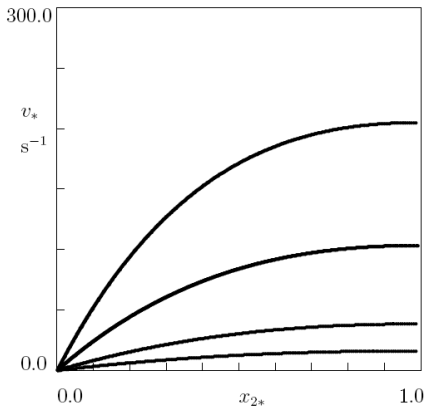

Figure 15: Velocity v_* versus dimensionless coordinate x_{2*}. Solid lines: results of numerical simulation for steady Poiseuille flow at $T = 150$ °C with $\Delta P_* = 20$, 40, 80, and 120 kPa, from bottom to top, respectively.

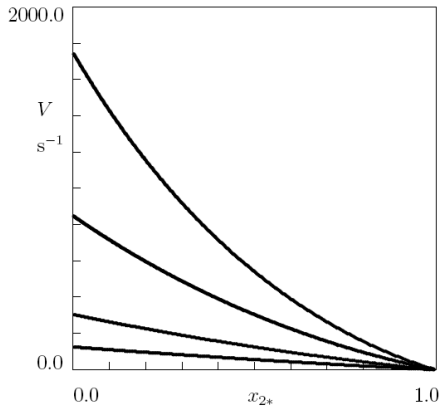

Figure 16: Velocity gradient V versus dimensionless coordinate x_{2*}. Solid lines: results of numerical simulation for steady Poiseuille flow at $T = 210$ °C with $\Delta P_* = 20$, 40, 80, and 120 kPa, from bottom to top, respectively.

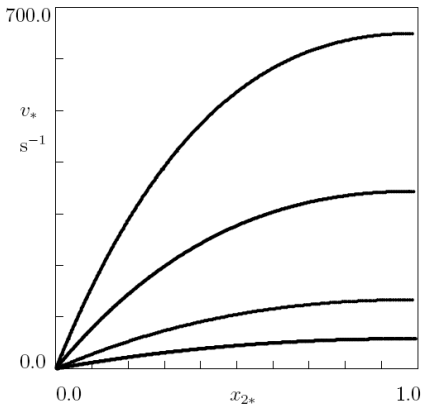

Figure 17: Velocity v_* versus dimensionless coordinate x_{2*}. Solid lines: results of numerical simulation for steady Poiseuille flow at $T = 210$ °C with $\Delta P_* = 20$, 40, 80, and 120 kPa, from bottom to top, respectively.

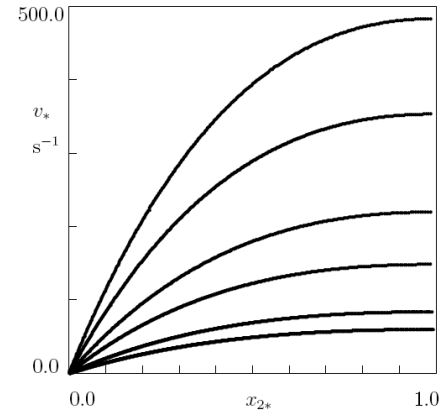

Figure 18: Velocity v_* versus dimensionless coordinate x_{2*}. Solid lines: results of numerical simulation for steady Poiseuille flow with $\Delta P_* = 100$ kPa at the temperatures $T = 120$, 130, 150, 170, 190, and 210 °C, from bottom to top, respectively.

strate that the dependencies $V(x_{2*})$ are close to linear (the latter correspond to the classical solution) at ΔP_*=20 kPa, and they become substantially nonlinear with an increase in ΔP_*. The velocity gradient V strongly grows with ΔP_*, in particular, at relatively small values of x_{2*}, that is near the wall x_2=0.

According to Figs. 15 and 17, shape of the curves $v_*(x_{2*})$ is parabolic at the smallest value of ΔP_*. When ΔP_* increases, the curves $v_*(x_{2*})$ deviate from this pattern, and a pronounced growth of the maximum velocity is observed. This growth is in accord with the results of molecular-dynamics simulations reported in [62]. Comparison of Figs. 15 and 17 shows a strong increase of the steady velocity with temperature.

To evaluate this growth, numerical simulation is performed of Eqs. (8.21)–(8.23), (8.26), and (8.27) for ΔP_*=100 kPa at all temperatures T under consideration. The results are presented in Fig. 18, where the steady velocity v_* is plotted versus dimensionless coordinate x_{2*}. This figure shows that the maximum velocity increases by a factor of 8, when temperature T grows from 120 to 210 °C.

9 Concluding remarks

Two series of rheological tests (small-amplitude oscillatory tests in the frequency-sweep mode and start-up shear tests with various strain rates) have been performed on a thermoplastic-elastomer melt at various temperatures T ranging from 120 °C to 210 °C.

Constitutive equations are developed for the mechanical response of a melt at arbitrary three-dimensional deformations with finite strains. The melt is treated as an incompressible, inhomogeneous, non-affine network of chains, where junctions between chains (physical cross-links and entanglements) slide with respect to their reference positions. The stress–strain relations are derived by using the laws of thermodynamics. For an isothermal deformation, these equations involve 5 adjustable parameters. The number of material constants increases up to 8 for non-isothermal deformation programs.

Material constants are found by fitting the experimental data. It is demonstrated that the constitutive equations adequately describe the observations, and the adjustable parameters change consistently with temperature. To validate the model, two additional series of rheological tests have been performed. An acceptable agreement is revealed between experimental data in these tests and predictions of the model. It is shown that the results of numerical analysis obey the Cox–Merz rule with a high level of accuracy.

As an application, Poiseuille flow of TPE melt in a channel is analyzed. A set of nonlinear differential-algebraic equations is developed for the steady flow velocity. These equations are solved numerically with the material parameters found by matching the observations. It is demonstrated that the steady velocity is strongly affected by temperature and pressure gradient. The velocity profile is parabolic at small pressure gradients (which is typical of the classical solution), and it strongly deviates from the

parabolic law with growth of pressure gradient. An increase in temperature (in the range of temperatures under consideration) leads to the growth of maximum velocity by several times.

Acknowledgements

Financial support from the European Commission under the project Nanotough 213436 is gratefully acknowledged.

References

[1] A. I. LEONOV, *Nonequilibrium thermodynamics and rheology of viscoelastic polymer media*, Rheol. Acta., 15 (1976), pp. 85–98.
[2] M. W. JOHNSON AND D. SEGALMAN, *A model for viscoelastic fluid behavior which allows non-affine deformation*, J. Non-Newton. Fluid., 2 (1977), pp. 255–270.
[3] N. PHAN THIEN AND R. I. TANNER, *A new constitutive equation derived from network theory*, J. Non-Newton. Fluid., 2 (1977), pp. 353–365.
[4] M. H. WAGNER, *Prediction of primary normal stress difference from shear viscosity data using a single integral constitutive equation*, Rheol. Acta., 16 (1977), pp. 43–50.
[5] H. GIESEKUS, *A simple constitutive equation for polymer fluids based on the concept of deformation-dependent tensorial mobility*, J. Non-Newton. Fluid., 11 (1982), pp. 69–109.
[6] K. R. GEURTS AND L. E. WEDGEWOOD, *A finitely extensible network strand model with nonlinear backbone forces and entanglement kinetics*, J. Chem. Phys., 106 (1997), pp. 339–346.
[7] T. C. B. MCLEISH AND R. G. LARSON, *Molecular constitutive equations for a class of branched polymers: The pom–pom model*, J. Rheol., 42 (1998), pp. 81–110.
[8] C. C. HUA, J. D. SCHIEBER AND D. C. VENERUS, *Segment connectivity, chain-length breathing, segmental stretch, and constraint release in reptation models. 3. Shear flows*, J. Rheol., 43 (1999), pp. 701–717.
[9] M. H. WAGNER, P. RUBIO AND H. BASTIAN, *The molecular stress function model for polydisperse polymer melts with dissipative convective constraint release*, J. Rheol., 45 (2001), pp. 1387–1412.
[10] C. GABRIEL AND H. MUNSTEDT, *Creep recovery behavior of metallocene linear low-density polyethylenes*, Rheol. Acta., 38 (1999), pp. 1435–1528.
[11] S. E. BIN WADUD AND D. G. BAIRD, *Shear and extensional rheology of sparsely branched metallocene-catalyzed polyethylenes*, J. Rheol., 44 (2000), pp. 1151–1167.
[12] C. GABRIEL AND H. MUNSTEDT, *Influence of long-chain branches in polyethylenes on linear viscoelastic flow properties in shear*, Rheol. Acta., 41 (2002), pp. 232-244.
[13] A. H. DEKMEZIAN, J. B. P. SOARES, P. JIANG, C. A. GARCIA-FRANCO, W. WENG, H. FRUITWALA, T. SUN AND D. SARZOTTI, *Characterization and modeling of metallocene-based branch-block copolymers*, Macromolecules., 35 (2002), pp. 9586-9594.
[14] D. J. LOHSE, S. T. MILNER, L. J. FETTERS, M. XENIDOU, N. HADJICHRISTIDIS, R. A. MENDELSON, C. A. GARCIA-FRANCO AND M. K. LYON, *Well defined model long chain branched polyethylene. 2. Melt rheological behavior*, Macromolecules., 35 (2002), pp. 3066–3075.
[15] B. PATHAM AND K. JAYARAMAN, *Creep recovery of random ethylene-octene copolymer melts with varying comonomer content*, J. Rheol., 49 (2005), pp. 989–999.

[16] C. A. GARCIA-FRANCO, B. A. HARRINGTON AND D. J. LOHSE, *On the rheology of ethylene-octene copolymers*, Rheol. Acta., 44 (2005), pp. 591–599.
[17] W. QIYE, L. PENG, M. JINGXIA, Z. NA, A. PENG AND W. JINGAN, *The rheological behavior of EPDM Nordel IP and POE Engage produced by CGC and INSITETM technology*, J. Appl. Polym. Sci., 101 (2006), pp. 2847–2853.
[18] I. A. HUSSEIN, T. HAMEED AND M. C. WILLIAMS, *Influence of molecular structure on the rheology and thermorheology of metallocene polyethylenes*, J. Appl. Polym. Sci., 102 (2006), pp. 1717–1728.
[19] F. J. STADLER, C. GABRIEL AND H. MUNSTEDT, *Influence of short-chain branching of polyethylenes on the temperature dependence of rheological properties in shear*, Macromol. Chem. Phys., 208 (2007), pp. 2449–2454.
[20] M. S. GREEN AND A. V. TOBOLSKY, *A new approach to the theory of relaxing polymeric media*, J. Chem. Phys., 14 (1946), pp. 80–92.
[21] F. TANAKA AND S. F. EDWARDS, *Viscoelastic properties of physically cross-linked networks. Transient network theory*, Macromolecules., 25 (1992), pp. 1516–1523.
[22] M. ZATLOUKAL, *Differential viscoelastic constitutive equations for polymer melts in steady shear and elongational flows*, J. Non-Newton. Fluid Mech., 113 (2003), pp. 209–227.
[23] M .M. DENN, *Extrusion instabilities and wall slip*, Annu. Rev. Fluid. Mech., 33 (2001), pp. 265–287.
[24] A. N. MOROZOV AND W. VAN SAARLOOS, *An introductory essay on subcritical instabilities and the transition to turbulence in visco-elastic parallel shear flows*, Phys. Rep., 447 (2007), pp. 112–143.
[25] C. METIVIER AND C. NOUAR, *On linear stability of Rayleigh–Benard Poiseuille flow of viscoplastic fluids*, Phys. Fluids., 20 (2008), No. 104101.
[26] M. RENARDY, *Stress modes in linear stability of viscoelastic flows*, J. Non-Newton. Fluid Mech., 159 (2009), pp. 137–140.
[27] K. R. RAJAGOPAL AND R. K. BHATNAGAR, *Exact solutions for some simple flows of an Oldroyd–B fluid*, Acta. Mech., 113 (1995), pp. 233–239.
[28] T. HAYAT, A. M. SIDDIQUI AND S. ASGHAR, *Some simple flows of an Oldroyd–B fluid*, Int. J. Eng. Sci., 39 (2001), pp. 135–147.
[29] A. F. KHADRAWI, M. A. AL-NIMR AND A. OTHMAN, *Basic viscoelastic fluid flow problems using the Jeffreys model*, Chem. Eng. Sci., 60 (2005), pp. 7131–7136.
[30] A. COHEN AND B. CASWELL, *A procedure for calculation of the Wagner model velocity profile in the Poiseuille flow*, Rheol. Acta., 27 (1988), pp. 202–204.
[31] J. J. VAN SCHAFTINGEN AND M. J. CROCHET, *Analytical and numerical solution of the Poiseuille flow of the Johnson–Segalman fluid*, J. Non-Newton. Fluid Mech., 18 (1985), pp. 335–351.
[32] K. R. RAJAGOPAL AND I. J. RAO, *Some simple flows of a Johnson–Segalman fluid*, Acta. Mech., 132 (1999), pp. 209–219.
[33] J. Y. YOO AND H. CH. CHOI, *On the steady simple shear flows of the one-mode Giesekus fluid*, Rheol. Acta., 28 (1989), pp. 13–24.
[34] G. SCHLEINIGER AND R. J. WEINACHT, *Steady Poiseuille flow for a Giesekus fluid*, J. Non-Newton. Fluid Mech., 40 (1991), pp. 79–102.
[35] I. DAPRA AND G. SCARPI, *Couette–Poiseuille flow of the Giesekus model between parallel plates*, Rheol. Acta., 48 (2009), pp. 117–120.
[36] M. A. HULSEN, *Some properties and analytical expressions for plane flow of Leonov and Giesekus models*, J. Non-Newton. Fluid Mech., 30 (1988), pp. 85–92.
[37] M. SILINE AND A. I. LEONOV, *On flows of viscoelastic liquids in long channels and dies*, Int.

J. Eng. Sci., 39 (2001), pp. 415–437.
[38] P. J. OLIVEIRA AND F. T. PINHO, *Analytical solution for fully-developed channel and pipe flow of Phan-Thien–Tanner fluids*, J. Fluid. Mech., 387 (1999), pp. 271–280.
[39] P. J. OLIVEIRA, *An exact solution for tube and slit flow of a FENE–P fluid*, Acta. Mech., 158 (2002), pp. 157–167.
[40] D. O. A. CRUZ AND F . T. PINHO, *Fully-developed pipe and planar flows of multimode viscoelastic fluids*, J. Non-Newton. Fluid Mech., 141 (2007), pp. 85–98.
[41] Y. WANG, *Time-dependent Poiseuille flows of visco-elasto-plastic fluids*, Acta. Mech., 186 (2006), pp. 187–201.
[42] C. J. HEATON, *Linear instability of annular Poiseuille flow*, J. Fluid. Mech., 610 (2008), pp. 391–406.
[43] Y. -L. CHEN AND K. -Q. ZHU, *Couette–Poiseuille flow of Bingham fluids between two porous parallel plates with slip conditions*, J. Non-Newton. Fluid Mech., 153 (2008), pp. 1–11.
[44] E. TALIADOROU, G. C. GEORGIOU AND I. MOULITSAS, *Weakly compressible Poiseuille flows of a Herschel–Bulkley fluid*, J. Non-Newton. Fluid Mech., 158 (2009), pp. 162–169.
[45] J. HRON, J. MALEK AND K. R. RAJAGOPAL, *Simple flow of fluids with pressure dependent viscosities*, P. R. Soc. London. A, 457 (2001), pp. 1603–1622.
[46] H. EYRING, *Viscosity, plasticity, and diffusion as examples of absolute reaction rates*, J. Chem. Phys., 4 (1936), pp. 283–291.
[47] B. DERRIDA, *Random-energy model: limit of a family of disordered models*, Phys. Rev. Lett., 45 (1980), pp. 79–92.
[48] R. PIVOKONSKY, M. ZATLOUKAL AND P. FILIP, *On the predictive/fitting capabilities of the advanced differential constitutive equations for branched LDPE melts*, J. Non-Newton. Fluid Mech., 135 (2006), pp. 58–67.
[49] R. I. TANNER, Engineering Rheology, Clarendon Press, Oxford, 1992.
[50] C. A. D. LEGUY, E. M. H. BOSBOOM, A. P. G. HOEKS AND F. N. VAN DE VOSSE, *Model-based assessment of dynamic arterial blood volume flow from ultrasound measurements*, Med. Biol. Eng. Comput., 47 (2009), pp. 641–648.
[51] T. M. SQUIRES AND S. R. QUAKE, *Microfluidics: Fluid physics at the nanoliter scale*, Rev. Mod. Phys., 77 (2005), pp. 977–1026.
[52] Z. LI, *Surface effects on friction-induced fluid heating in nanochannel flows*, Phys. Rev. E, 79 (2009), No. 026312.
[53] D. GLOSS AND H. HERWIG, *Microchannel roughness effects: A close-up view*, Heat. Transfer. Eng., 30 (2009), pp. 62–69.
[54] J. SERVANTIE AND M. MULLER, *Temperature dependence of the slip length in polymer melts at attractive surfaces*, Phys. Rev. Lett., 101 (2008), No. 026101.
[55] M. MULLER, C. PASTORINO AND J. SERVANTIE, *Flow, slippage and a hydrodynamic boundary condition of polymers at surfaces*, J. Phys-Condens. Mat., 20 (2008), No. 494225.
[56] M. MULLER, C. PASTORINO AND J. SERVANTIE, *Hydrodynamic boundary condition of polymer melts at simple and complex surfaces*, Comput. Phys. Commun., 180 (2009), pp. 600–604.
[57] N. ROQUET AND P. SARAMITO, *An adaptive finite element method for viscoplastic flows in a square pipe with stick-slip at the wall*, J. Non-Newton. Fluid Mech., 155 (2008), pp. 101–115.
[58] M. H. KHADEM, M. SHAMS AND S. HOSSAINPOUR, *Numerical simulation of roughness effects on flow and heat transfer in microchannels at slip flow regime*, Int. Comm. Heat Mass Trans., 36 (2009), pp. 69–77.
[59] R. D. BRANAM AND M. M. MICCI, *Comparison of wall models for the molecular dynamics simulation of microflows*, Nanosc. Microsc. Therm. Eng., 13 (2009), pp. 1-12.
[60] P. A. THOMPSON AND M. O. ROBBINS, *Shear flow near solids: Epitaxial order and flow*

boundary conditions, Phys. Rev. A, 41 (1990), pp. 6830–6837.

[61] T. MA AND S. WANG, *Boundary-layer and interior separations in the Taylor-Couette-Poiseuille flow*, J. Math. Phys., 50 (2009), No. 033101.

[62] J. CASTILLO-TEJAS, J. F. J. ALVARADO, G. GONZALEZ-ALATORRE, G. LUNA-BARSENAS, I. C. SANCHEZ, R. MACIAS-SALINAS AND O. MANERO, *Nonequilibrium molecular dynamics of the rheological and structural properties of linear and branched molecules. Simple shear and Poiseuille flows; instabilities and slip*, J. Chem. Phys., 123 (2005), No. 054907.